

Communication

Impact of Nitric Oxide on the Surface Properties of Selected Polymers

Moritz Köglmaier ^{1,*}, Anja Caspari ², Stefan Michel ², Günter K. Auernhammer ² and Werner Kunz ¹

¹ Institute of Physical and Theoretical Chemistry, University of Regensburg, 93040 Regensburg, Germany; werner.kunz@ur.de

² Institute of Physical Chemistry and Polymer Physics, Leibniz-Institut für Polymerforschung Dresden e.V., 01069 Dresden, Germany; caspari@ipfdd.de (A.C.); michel@ipfdd.de (S.M.); auernhammer@ipfdd.de (G.K.A.)

* Correspondence: moritz.koeglmaier@ur.de

Abstract: The change in the surface properties of polymer materials used in an extracorporeal membrane oxygenation (ECMO) device due to nitric oxide (NO) treatment was characterized by zeta-potential and dynamic contact-angle measurements. FTIR-ATR was used to determine the stability of these effects during liquid contact. Polymethyl pentene (PMP), methyl methacrylate acrylonitrile butadiene styrene (MABS), and polyurethane (PU) were investigated. The polymer materials were treated with NO (1000 ppm) for 17 h. The samples for FTIR-ATR measurements were submerged in water or physiological sodium chloride solution for 120 and 240 h after the end of the gas treatment. PMP showed no changes at all. MABS showed decreased contact-angles and increased contact-angle hysteresis. In contrast, PU showed decreased contact-angles and a shift in its zeta-potential curve, indicating a more hydrophilic and acidic surface. The FTIR-ATR measurements showed a slight decrease in the signal intensities after liquid contact. The results indicated an improvement in the liquid contact properties of MABS and the PU due to increased surface hydrophilicity caused mainly by the adsorbed nitric acid (HNO₃) molecules formed by the NO treatment. The results presented in this paper point towards a simple and complication-free method of introducing NO into an ECMO circuit.

Keywords: FTIR-ATR; zeta-potential; dynamic contact-angle; surface properties; ECMO



Academic Editors: Iole Vozza and Piotr Gas

Received: 18 December 2024

Revised: 7 February 2025

Accepted: 26 February 2025

Published: 1 March 2025

Citation: Köglmaier, M.; Caspari, A.; Michel, S.; Auernhammer, G.K.; Kunz, W. Impact of Nitric Oxide on the Surface Properties of Selected Polymers. *Appl. Sci.* **2025**, *15*, 2646. <https://doi.org/10.3390/app15052646>

Copyright: © 2025 by the authors. Licensee MDPI, Basel, Switzerland. This article is an open access article distributed under the terms and conditions of the Creative Commons Attribution (CC BY) license (<https://creativecommons.org/licenses/by/4.0/>).

1. Introduction

Extracorporeal membrane oxygenation (ECMO) is a clinical technique used to support patients in critical conditions such as heart and lung transplantations or acute respiratory distress syndrome (ARDS). Blood is taken from the patient's venous system, pumped through a so-called oxygenator, and then infused back into the patient's venous or arterial system [1,2]. One of the common issues of such a system, particularly in cases of long-term patient support, is the formation of thrombi in the ECMO system [3,4]. Progression in the size of the formed thrombi can ultimately lead to a failure of the ECMO circuit [5,6]. Replacing the ECMO circuit causes a gap in patient support, blood loss, and blood dilution, increasing the risk for already compromised patients [3,7]. To suppress the thrombus formation and increase the life span of the ECMO circuit, the addition of nitric oxide (NO) could be a promising pathway. NO is a reactive molecule that occurs naturally in the human body and is part of the blood clotting mechanism as it is released by aggregated blood platelets to limit further aggregation [8,9].

Research investigating the chemical impact of NO treatment on the polymers used in the oxygenator was previously published by some of the authors of this paper [10].

Using Fourier transform infrared attenuated total reflection (FTIR-ATR) spectroscopy, the formation of several functional groups was elucidated. NO reacted with the surrounding air to form NO_2 , which reacted with the air humidity to form nitric acid (HNO_3). Both of these compounds reacted with the polymers to form nitro and nitrate ester groups. HNO_3 was also adsorbed on the polymer surfaces [10].

This communication is meant to further expand the understanding of the interaction between NO and the polymer surfaces investigated in the previous paper. Zeta-potential and dynamic contact-angle measurements were conducted to elucidate the surface properties of the materials and the impact of NO on them. Polymethyl pentene (PMP), methyl methacrylate acrylonitrile butadiene styrene (MABS), and polyurethane (PU) were chosen because all three materials are in contact with blood during the application of the oxygenator (Figure 1). The FTIR-ATR experiments discussed in this communication aimed to expand on the stability measurements under dry conditions discussed in the previous paper [10]. The experiments discussed here were performed to quantify the influence of liquid contact on the effects of NO treatment. The possibility of analyzing both the hydrophilicity and the zeta-potential is of practical interest in this context, as the surface properties of the polymers could influence their blood contact properties [1,11]. The overall goal of the research presented in this and the previous paper [10] is to enable the use of NO as an additive to the sweep gas of an ECMO circuit to suppress thrombus formation and increase its longevity. These increases have historically been achieved through substantial modifications to the oxygenator and the pump both in terms of materials and geometry [12–14]. The addition of coagulation suppressants such as heparin or argatroban has been another method of achieving this increased longevity [12,15]. The addition of NO to the sweep gas would, in contrast, represent a simpler way to increase the longevity of the ECMO circuit, requiring little to no modification to the circuit itself [16]. At the same time, NO would allow for a more continuous addition of the coagulation suppressant than compounds like heparin. NO has been trialed in ECMO circuits and other implants, being released from specialized materials. The results with these materials were positive overall with significant improvements to the thrombotic properties [17,18]. The use of NO as a sweep gas additive has so far produced inconclusive results that warrant further research [19,20].

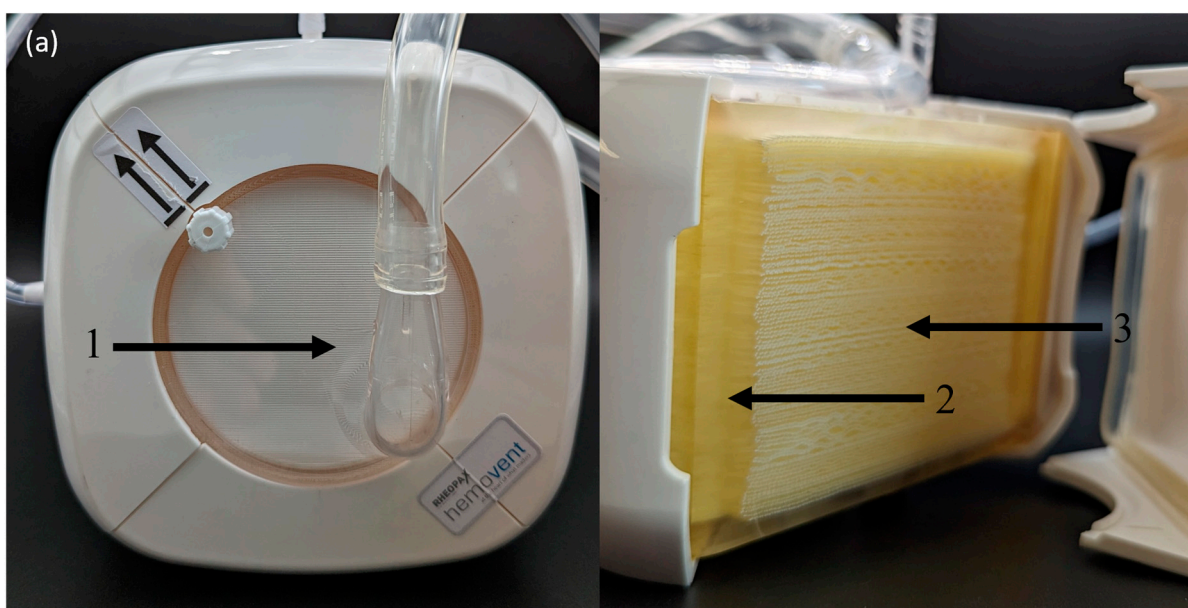


Figure 1. Cont.

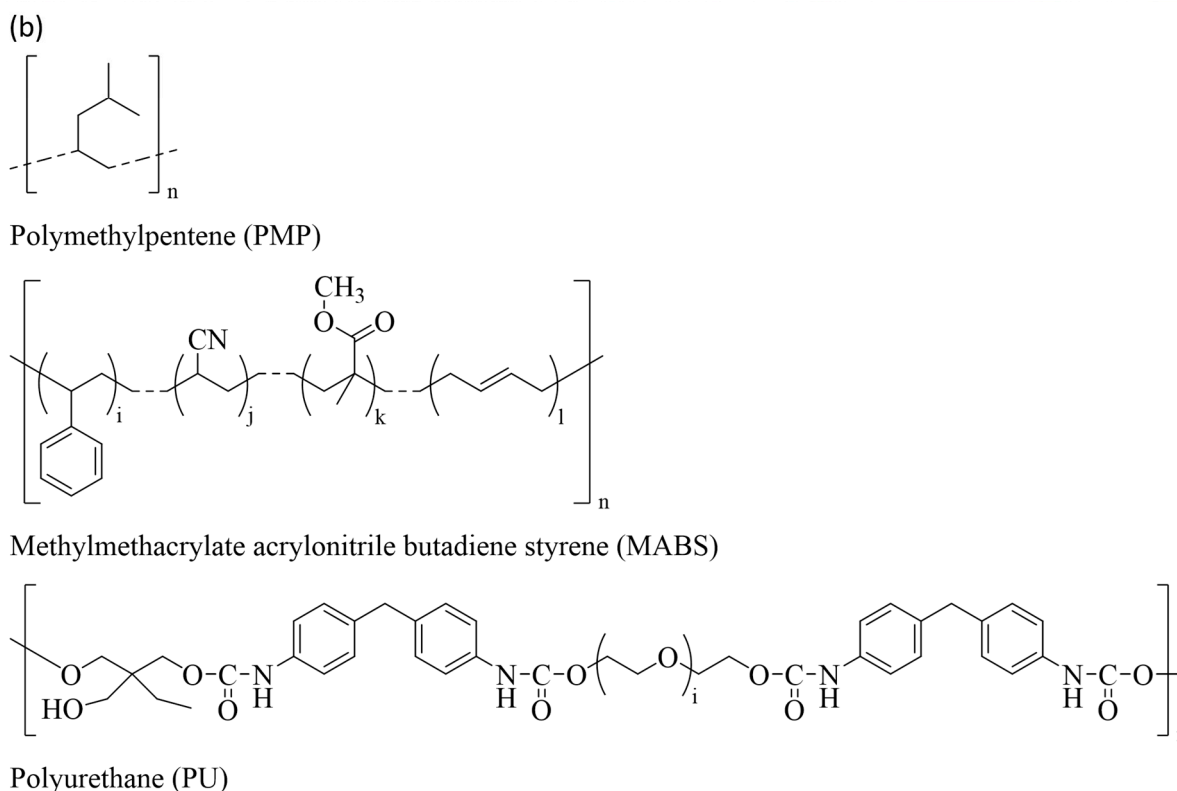


Figure 1. (a) Overview of the locations of the sample materials in the oxygenator: (1) Outlet plate (MABS) with hollow fiber membranes (PMP) visible behind it. (2) PU material. (3) Hollow fiber membrane ends encased in PU. (b) Overview of the polymers investigated in this paper [21–23]. A version of this figure was first published in the *Journal of Polymer Research*, 31 (261), 2024, by Springer Nature [10].

2. Experimental Section

2.1. Chemicals and Materials

NO (1000 ppm in N₂) was purchased from basi Schöberl GmbH & Co. KG (Rastatt, Germany). As hollow fiber membranes, Membrana OXYPLUS, type PMP 90/200 (3M Deutschland GmbH, Wuppertal, Germany), were used. The MABS samples consisted of Terlux HD 2802 (INEOS Styrolution Group GmbH, Frankfurt am Main, Germany). PU consisted of methylene diphenyl diisocyanate (Biresin DH41 Komp. B, Sika Deutschland GmbH, Stuttgart, Germany) and trimethylolpropane (Biresin DH404 Komp. A, sika Deutschland GmbH, Stuttgart, Germany). Material samples of the gas exchanger components, including hollow fiber membranes, inlet/outlet caps, and (PU) sheets, were provided by Hemovent GmbH (Aachen, Germany). All sample materials were commercial products potentially containing residues of additives used in the production process, potentially influencing the results.

2.2. NO Treatment of the Gas Exchanger Materials

The polymer samples were treated with 1000 ppm NO in nitrogen. This was the highest available concentration, chosen to maximize the impact of the NO treatment. In the first step, the polymer materials were cut down to a sample size of two by one centimeters in the case of MABS and the PU sheets. Samples with a fiber length of around four centimeters were cut from hollow fiber mats for the PMP samples. The samples were placed in a chamber. The NO gas mixture was added to the chamber at a flow rate of 2 L/min for ten minutes to displace the air from the chamber. After ten minutes, the chamber was closed, and the gas flow was stopped. The samples were left in the chamber overnight for 17 h.

2.3. Additional Sample Treatment

A part of the polymer samples was treated further to analyze the stability of the NO treatment effects in liquid contact. For this purpose, polymer samples were submerged in either Millipore water or a physiological sodium chloride solution (9 g/L NaCl in Millipore water). FTIR-ATR measurements were conducted directly after the NO treatment and after 120 and 240 h of submerging the samples in the respective liquid. The samples were dried in a desiccator for 24 h over silica gel between the submersion intervals and the FTIR-ATR measurements. The samples immersed in sodium chloride solution were washed with Millipore water before drying to stop salt deposition on the polymer surface. Both liquids were chosen for their simplicity. The sodium chloride solution was additionally selected due to its technical relevance as a priming liquid in ECMO applications [24].

2.4. FTIR-ATR Measurements

FTIR-ATR measurements were conducted using an Agilent Varian 670 IR spectroscope (Agilent Technologies Inc., Santa Clara, CA, USA), and a Pike Technologies GladiATR probe head (Pike Technologies, Fitchburg, WI, USA) was used to conduct the measurements. The dried polymer samples were pinned onto the diamond of the probe head using the integrated clamp to ensure complete and consistent coverage of the diamond surface. The sampling depth of this method ranges from 2 to 15 μm depending on both sample material and radiation wavelength [25]. The spectra were recorded with 16 scans at a resolution of 2 cm^{-1} . The spectral range was 4000 to 500 cm^{-1} . For both PMP and MABS, the signals caused by the NO treatment were also investigated in terms of peak height. For this purpose, the spectra were baseline-corrected and normalized using the signal located at 1466 cm^{-1} in the case of PMP and 1720 cm^{-1} for MABS. These signals were chosen based on their high intensity and consistency across different measurements. The highest data point determined the height of the signals.

2.5. Zeta-Potential Measurements

The zeta-potential measurements were conducted using a SurPASS 3 (Anton Paar, Graz, Austria). An adjustable gap cell was used for the MABS and the PU samples. The gap was set at approximately $100\text{ }\mu\text{m}$. The pressure range utilized extended from 600 to 200 mbar. Care was taken for both materials to analyze the same side of the samples to avoid inconsistencies. These measures were taken as surface morphology can impact zeta-potential measurements [26]. The PMP samples were analyzed using a cylindrical cell. A total of 150 mg of PMP was used in these measurements. The permeability index of the cell was approximately 100. A KCl solution with a concentration of 10^{-3} mol/L was used as the electrolyte. Measurements were conducted over a pH range of three to ten using HCl and KOH solutions with a concentration of 0.05 mol/L to adjust the pH. Two separate sample pairs were used per measurement to cover the pH range. Measurements of both treated and untreated polymer samples were conducted. The zeta-potential was calculated using the Helmholtz–Smoluchowski equation [27]:

$$\zeta = \frac{dU_s}{d\Delta p} \frac{\eta \kappa}{\epsilon \epsilon_0} \quad (1)$$

with ζ being the zeta-potential, U_s being the change in the streaming potential, $d\Delta p$ being the change in pressure difference, η being the dynamic viscosity of the liquid, κ being the specific conductivity of the bulk liquid, ϵ being the relative permittivity of the liquid, and ϵ_0 being the electrical permittivity of the vacuum.

2.6. Dynamic Contact-Angle Measurements

Dynamic contact-angle measurements were conducted using a Dataphysics OCA 35L (Dataphysics, Filderstadt, Germany). The results were analyzed using the software SCA202. For MABS and PU, the sessile drop method was used. The polymer surface's wettability was quantified by depositing a liquid droplet. The contact-angle θ between the droplet and the surface results from the interfacial tensions at the solid–vapor (γ_{sv}), solid–liquid (γ_{sl}), and liquid–vapor (γ_{lv}) interfaces. In ideal situations, the relationship between the surface tensions and the contact-angle is described by the Young equation [28]:

$$\cos \theta_Y = \frac{\gamma_{sv} - \gamma_{sl}}{\gamma_{lv}} \quad (2)$$

In practical situations, factors like surface roughness and chemical heterogeneities lead to the pinning of the three-phase contact line. In the measurements, only the advancing θ_A and receding contact-angle θ_R can be determined. The Young contact-angle θ_Y is between these two limits, such that $\theta_R \leq \theta_Y \leq \theta_A$. Samples with a size of two by one centimeters were prepared for the measurements. Analogous to the samples for the zeta-potential measurements, care was taken to ensure the consistency of surface morphology, as factors like surface roughness can have pronounced impacts on the results [29,30]. Millipore water was used as the droplet fluid. An initial volume of 5 μL of water was placed on the sample's surface. During the measurement of the advancing angle θ_A , 15 μL of water was added to the surface. All 20 μL of water was removed again from the polymer surface while measuring the receding contact-angle θ_R . Water was added and removed at a rate of 0.1 $\mu\text{L}/\text{s}$.

The Wilhelmy Method was employed to analyze the contact-angle of PMP. The advancing and receding contact-angles (θ_A , θ_R) were calculated using the Wilhelmy Equation [31,32]:

$$F_w = \pi d \gamma_{lv} \cos \theta \quad (3)$$

F_w is the measured force, d is the diameter of the fiber, and γ_{lv} is the liquid–vapor surface tension. Measurements with PMP were conducted using single fibers, which were approximately 40 mm long. The fibers were compressed on the lower end to keep water from entering the inside of the fibers. The fiber was inserted into a cuvette filled with Millipore water to a maximum depth of 12 mm at a rate of 6 mm/min and then withdrawn at equal speed to measure both advancing and receding contact-angles. The contact-angles were recorded on both sides of the droplet or the fiber and averaged. Three repeat measurements were conducted for all three polymer materials.

3. Results and Discussion

3.1. FTIR-ATR Stability Measurements

The NO treatment of PMP produced shallow signals, as shown in Figure 2. The analyzed signals were located at 3377, 1712, and 1642 cm^{-1} . These signals originated from the adsorption of HNO_3 to the polymer surface in the case of the signals 3377 and 1712 cm^{-1} , while the signal at 1642 cm^{-1} originated from the formation of nitrate ester groups [10,25,33]. Looking at the close-ups of the spectra shown in Figure 2a–d, it was qualitatively observable that all three signals decreased to the same level of the untreated sample after 120 h of immersion in either water or NaCl solution. The signal intensities were low overall compared to MABS (Figure 3e,f), which led to significant variations when analyzing the signal heights. Treating the PMP samples with Millipore water resulted in a decrease in signal intensity for both the signal at 3377 and 1712 cm^{-1} . The signal at 1630 cm^{-1} stayed stable (Figure 2e). The spectra of the samples immersed in physiological

NaCl solution showed a slightly different behavior. All three signals decreased steadily throughout the treatment at relatively similar rates (Figure 2f).

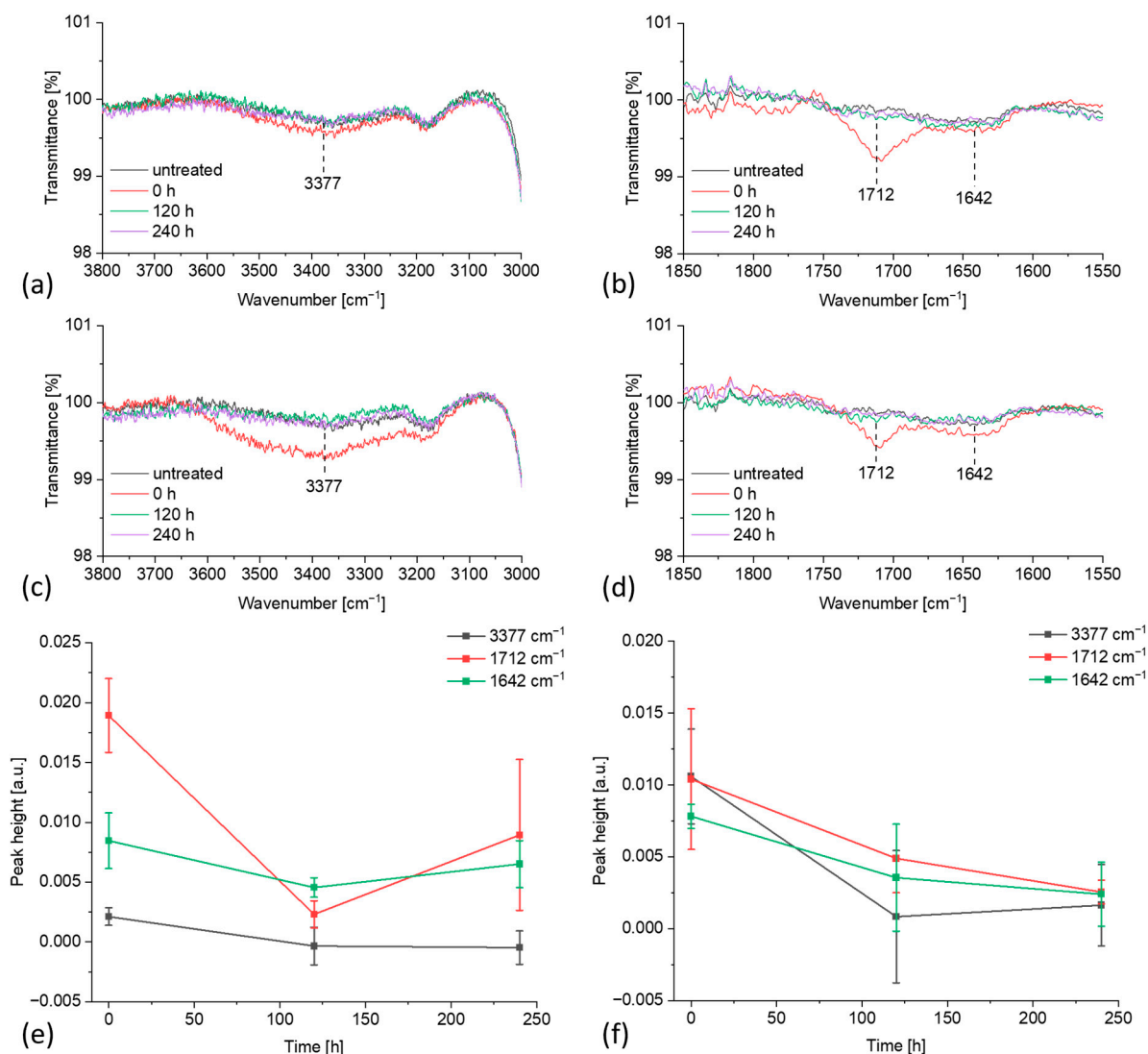


Figure 2. Results of the FTIR-ATR measurements of PMP. The samples were treated with NO (1000 ppm) for 17 h and subsequently immersed in Millipore water (a,b) and physiological sodium chloride solution (c,d). The samples were immersed for 120 (green) and 240 h (purple). The spectra are depicted in comparison to an untreated sample (black) and the sample directly after the NO treatment (red). (e) Peak heights at 3377 (black), 1712 (red), and 1642 cm⁻¹ (green) plotted against the immersion time in Millipore water and (f) physiological sodium chloride solution.

The NO treatment of MABS resulted in several clearly visible signals. For this investigation, the signals at 3443, 1630, and 1549 cm⁻¹ were the focus, as they were well separated from the signals caused by the polymer. These signals corresponded to adsorbed HNO₃ in the case of 3443 cm⁻¹, nitrate ester groups in the case of 1630 cm⁻¹, and nitro groups in the case of 1549 cm⁻¹ [10,25,33]. The samples immersed in Millipore water showed relatively constant peak heights, with only the signal at 1630 cm⁻¹ decreasing slightly from 0.15 to 0.14. The other two signals remained constant (Figure 3a,b,e). The immersion of the samples in physiological NaCl solution resulted in substantial decreases in the signals at 3443 and 1630 cm⁻¹. The signal at 3443 cm⁻¹ decreased from 0.015 to 0.003, while the signal at 1630 cm⁻¹ decreased from 0.14 to 0.10. Like the samples treated with water, the signal at 1549 cm⁻¹ remained constant (Figure 3c,d,f).

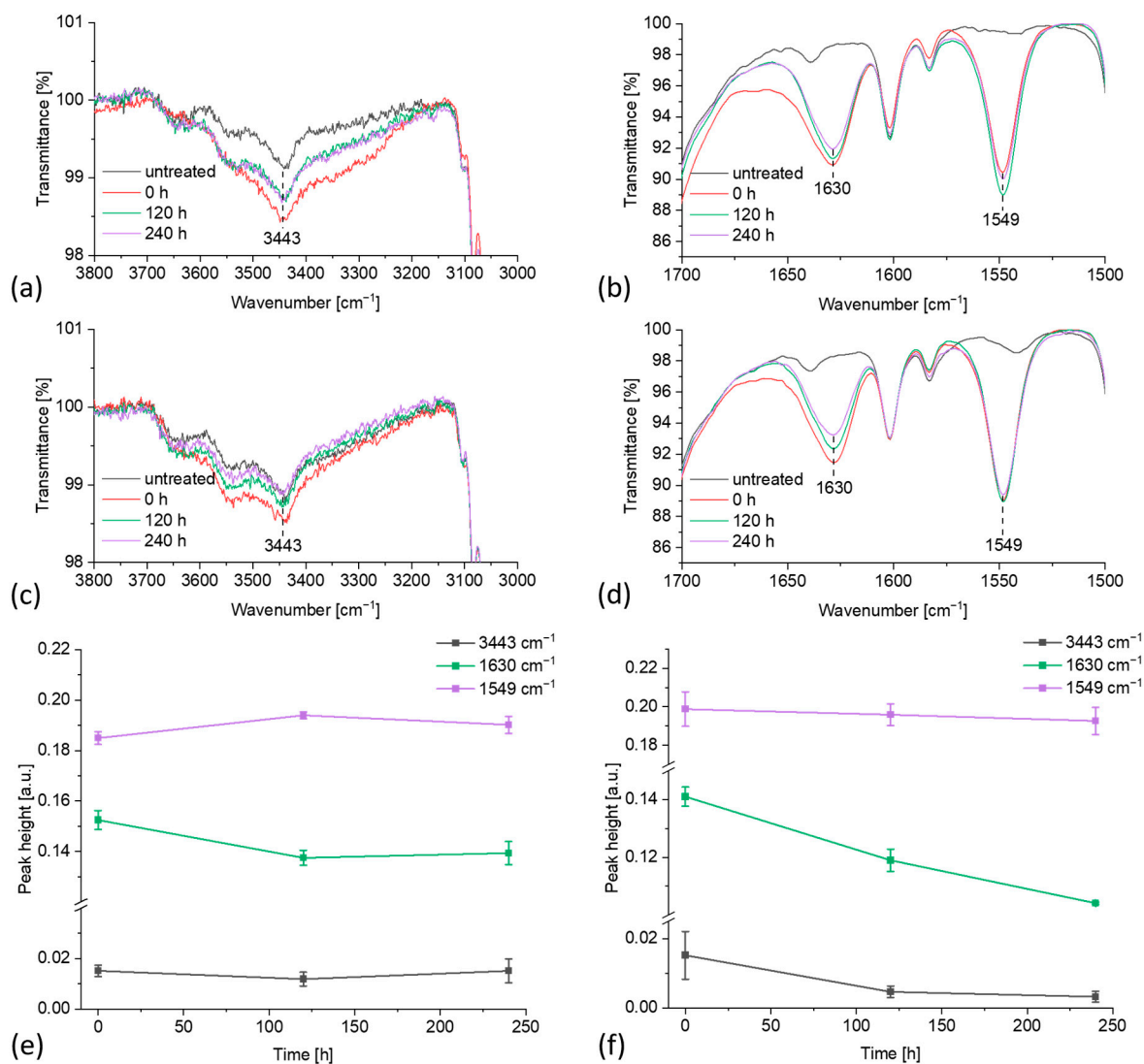


Figure 3. Results of the FTIR-ATR measurements of MABS. The samples were treated with NO (1000 ppm) for 17 h and subsequently immersed in Millipore water (a,b) and physiological sodium chloride solution (c,d). The samples were immersed for 120 h (green) and 240 h (purple). The spectra are depicted in comparison to an untreated sample (black) and the sample directly after the NO treatment (red). (e) Peak heights at 3443 (black), 1630 (green), and 1549 cm⁻¹ plotted against the immersion time in Millipore water and (f) physiological sodium chloride solution.

No peak height analysis was performed for PU, as the signals originating from the NO treatment and the PU signals overlapped too heavily (Figure 4). The signals' development at around 3480 and 1630 cm⁻¹ was observed qualitatively. These signals originated from the adsorption of HNO₃ in the case of 3480 cm⁻¹ and the formation of nitrate ester groups in the case of 1630 cm⁻¹ [25,33]. In the case of water and NaCl solution treatment, the signal at 3480 cm⁻¹ decreased to the same level as the untreated sample after only 120 h, with no additional changes. The signal at 1630 cm⁻¹ stayed stable in both cases.

As discussed in the previous publication [10], various possible mechanisms for forming the nitro and nitrate ester groups and the adsorption of HNO₃ have been discussed in the literature. The foundation for these mechanisms is the reaction of NO with oxygen forming nitrogen dioxide (NO₂) and the subsequent reaction of NO₂ with the moisture in the air forming HNO₃ (Figure 5) [34,35].

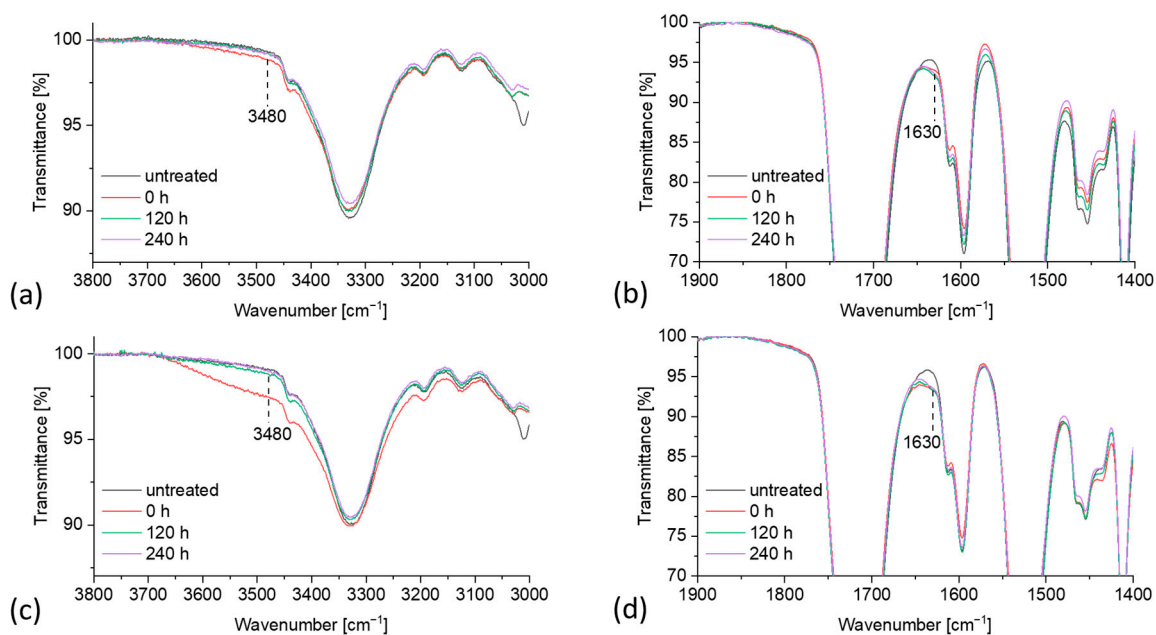
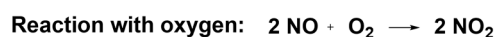


Figure 4. Results of the FTIR-ATR measurements of PU. The samples were treated with NO (1000 ppm) for 17 h and subsequently immersed in Millipore water (a,b) and physiological sodium chloride solution (c,d). The samples were immersed for 120 (green) and 240 h (purple). The spectra are depicted in comparison to an untreated sample (black) and to the sample directly after the NO treatment (red).



Reaction with air humidity:

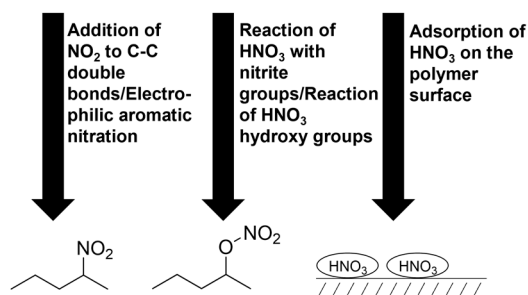
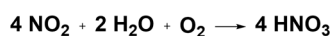


Figure 5. Schematic overview of the different mechanisms of interaction of NO with the polymer surfaces. A version of this figure was first published in the *Journal of Polymer Research*, 31 (261), 2024, by Springer Nature, as part of the Graphical Abstract [10].

These reactions leave both NO_2 and HNO_3 as the primary reactive compounds. The signals caused by HNO_3 were likely caused by excess HNO_3 molecules that did not participate in other reactions. Firstly, nitro groups can be formed through electrophilic addition of NO_2 to C-C double bonds, leading to nitro and nitrite ester groups forming in a 3:1 ratio (Scheme S1) [36,37]. This reaction could have occurred at the double bonds contained in the butadiene monomers of MABS and unreacted monomers of PMP based on the structures shown in Figure 2. Chain scission and crosslinking reactions are also possible pathways. Here, NO_2 abstracts a hydrogen atom from the polymer chain, causing the formation of a radical site. The radical site can then react with NO_2 through a side reaction, forming nitro groups, as seen in the final equation of Scheme S2. Points of attack were likely to be the carbamate groups of PU (Figure 1b) [38,39]. HNO_3 can lead to the formation of nitro groups through electrophilic aromatic nitration, where a hydrogen atom bound to an aromatic ring is substituted with a nitro group through a reaction with an intermediary

nitronium ion (Scheme S3) [40]. This reaction would have been possible at the aromatic rings of the styrene monomers of MABS or the MDI monomers of PU (Figure 1b). Nitrate ester groups can be formed through a secondary reaction of the electrophilic addition reaction. Here, the nitrite ester group decomposes, leaving an oxygen radical site with which NO_2 reacts to form the nitrate ester group (Scheme S4) [36,41]. The reaction of HNO_3 with hydroxy groups is also a possible mechanism. An intermediary nitronium ion binds to the oxygen atom of a hydroxy group, leading to the separation of the hydrogen and, subsequently, the formation of a nitrate ester group (Scheme S5) [42,43]. Potential attack points would have been the hydroxy groups of the trimethylolpropane monomers of PU (Figure 1b). This reaction could also occur as a follow-up reaction to an acid-catalyzed ester hydrolysis (Scheme S6). A potential attack point would have been the ester group of MABS. The formation of the functional groups discussed here was confirmed with both FTIR-ATR and XPS measurements in the previous publication [10].

PMP showed only a minor impact of NO (Figure 2). The small signals observable in the FTIR-ATR spectra disappeared quickly upon liquid contact (Figure 2c–f). PMP lacks any structural features mentioned in the discussion of the reaction mechanisms above. The polymer molecule consists of only carbon–carbon single bonds (Figure 1b), so the small signals visible in the FTIR-ATR spectra were most likely due to residual monomers in the samples.

MABS and PU showed clearly visible signals in the FTIR-ATR spectra, with much higher intensities than PMP. The liquid immersion experiments showed a clear difference between signals corresponding to covalently bound nitrate ester and nitro groups, respectively, and the signal corresponding to adsorbed HNO_3 molecules. The signal at $3480/3443\text{ cm}^{-1}$ decreased significantly over time for both MABS and PU, while the other signals retained much higher proportions of their original height (Figures 3e,f, and 4). The likely interpretation for this behavior is that the adsorbed HNO_3 molecules were washed away during the immersion in the liquid while the covalently bound functional groups remained on the surface. For PU, no differences between immersion in water and saline solution could be observed (Figure 4). Conversely, MABS showed a more substantial height dropoff of both the signal at 3443 and 1630 cm^{-1} with the saline solution (Figure 3e,f). The likeliest explanation for this difference in behavior would be the additional washing step before the drying process in the case of the saline solution, which led to more HNO_3 molecules being removed from the surface. For the nitrate ester groups, the decrease in signal heights after liquid immersion was likely due to acid-catalyzed hydrolysis, as both the Millipore water and the saline solution were slightly acidic due to CO_2 absorption from the atmosphere [44,45]. The faster dropoff in combination with the NaCl solution was likely again due to the samples being rinsed with Millipore water, as the salt concentration itself was too low to affect the reaction rates [46].

3.2. Zeta-Potential and Dynamic Contact-Angle Measurements

The dynamic contact-angle measurements showed no significant changes for PMP (Figure 6a). Meanwhile, measurements with MABS and PU showed substantial decreases in advancing and receding angles. The advancing angle decreased from 103 to 74 degrees for MABS, while the receding angle decreased from 64 to below 10 degrees. The contact-angle hysteresis $\theta_A - \theta_R$ increased from 39 to 64 degrees (Figure 6b). For PU, the advancing angle decreased from 106 to 68 degrees, and the receding angle decreased from 49 to 15 degrees. The contact-angle hysteresis showed a minor decline from 57 to 53 degrees (Figure 6c).

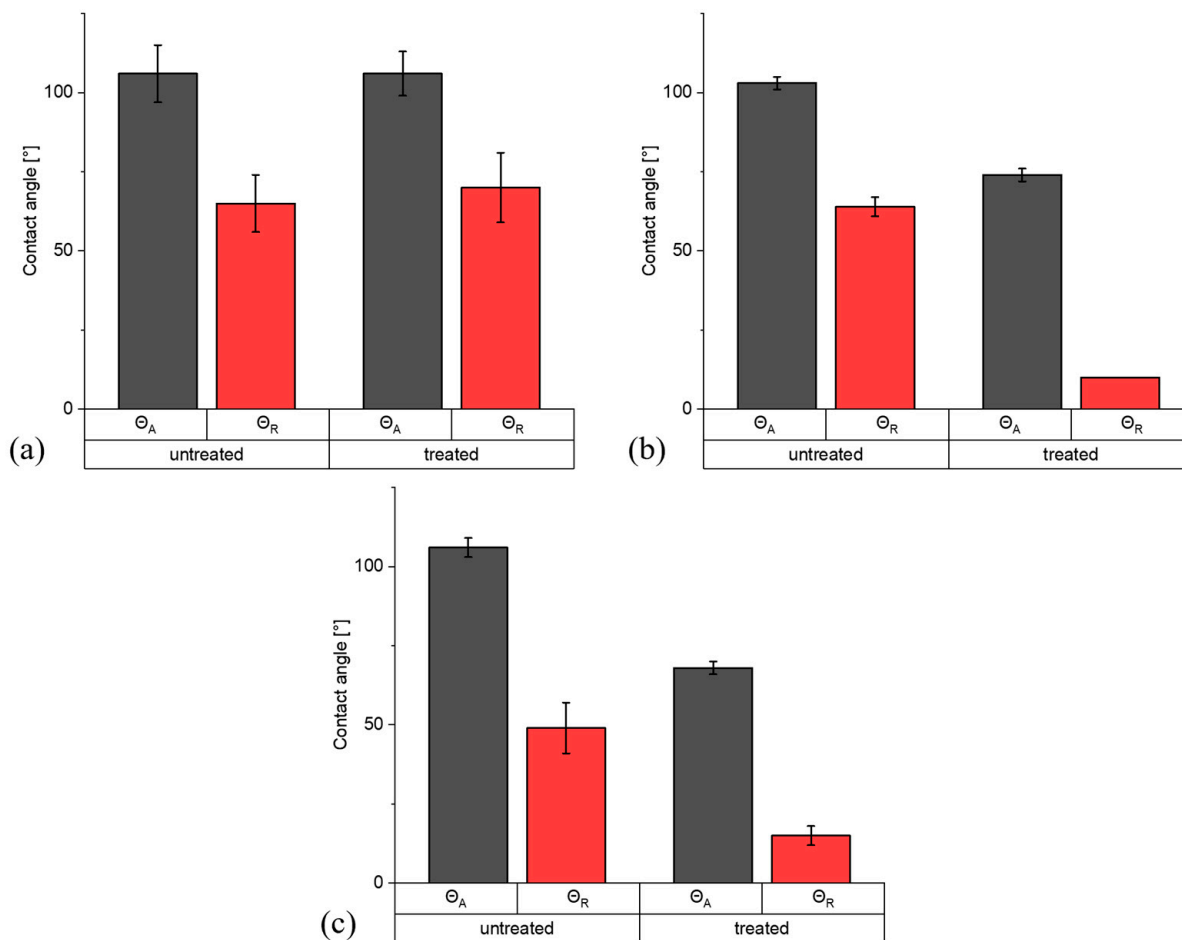


Figure 6. Dynamic contact-angle measurements of both the advancing contact-angle θ_A (gray) and the receding contact-angle θ_R (red) of (a) PMP, (b) MABS, and (c) PU. Each material was measured in its untreated state and after treatment with NO (1000 ppm) for 17 h.

The decrease in the contact-angles indicated an increase in hydrophilicity of the surfaces of both MABS and PU caused by the formation of the nitrate ester and nitro groups and the adsorption of the HNO_3 groups (Figure 6). The adsorption of HNO_3 was likely the major contributor to the changes in contact-angle, given the more polar nature of the HNO_3 molecules compared to the nitro and nitrate ester functional groups. This attribution was further supported by the streaming potential results obtained for PU (Figure 7c), which are discussed in the paragraphs following Figure 7. There are several known sources of contact-angle hysteresis. The important factors in this case are swelling, surface roughness, and chemical heterogeneity [29,47–49]. Swelling and surface roughness could be neglected when comparing untreated and treated samples, as these factors were roughly constant between samples. Therefore, the most likely influencing factor was chemical heterogeneity. MABS is a copolymer consisting of four monomers (methyl methacrylate, acrylonitrile, butadiene, and styrene) (Figure 1b). As discussed in Section 3.1, the likely attack points for both NO_2 and HNO_3 were the double bonds of the butadiene monomers, the phenyl group of the styrene monomers, and the ester groups of methyl methacrylate monomers. No reactions occurred with acrylonitrile monomers due to their lack of suitable functional groups. This meant that nitro and nitrate ester groups only developed on three of the four monomers, increasing chemical heterogeneity as these functional groups were not formed evenly along the MABS molecules. The HNO_3 molecules likely preferentially adsorbed close to monomers with polar functional groups such as methyl methacrylate, again increasing chemical heterogeneity. With PU, the possible interaction sites were

the hydroxy groups of trimethylolpropane and the aromatic rings of the MDI monomers (Figure 1b). The more strictly defined structure of the PU polymer, with alternating polyol and diisocyanate monomers, led to a more even distribution of the functional groups caused by the gas treatment across the PU molecules, leading to no minor increase in chemical heterogeneity. The same was true for the adsorption of HNO_3 , which, for the same reasons, also likely occurred more uniformly across the surface of the PU samples. In contrast to MABS and PU, PMP possessed no functional groups or structural features that could interact with the treatment gas or facilitate the adsorption of HNO_3 (Figure 1b). This was confirmed by the FTIR-ATR results in Figure 3 and the previous publication [10]. This also meant that the surface concentration of HNO_3 was too low to affect the contact-angles of the PMP surface.

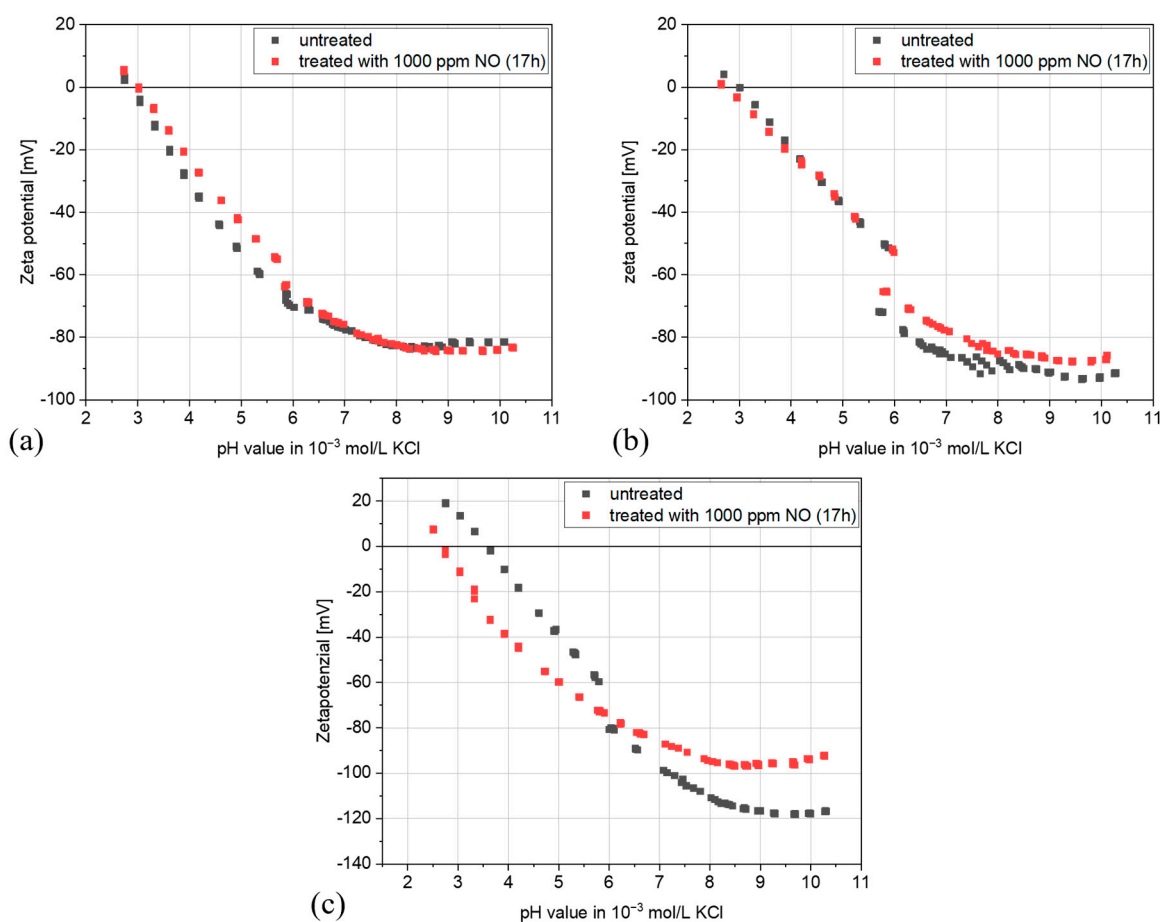


Figure 7. Zeta-potential measurements of (a) PMP, (b) MABS, and (c) PU. Each material was measured both in its untreated state (gray) and after treatment with NO (1000 ppm) for 17 h (red).

Both sample materials reached the IEP at a pH of approximately three (Figure 7a,b). For PU, the zeta-potential measurements showed significant differences between the treated and untreated samples (Figure 7c). The untreated PU samples showed a zeta-potential curve typical for uncharged polymers. The curve decreased steeply with increasing pH values and no plateau formation at higher pH values, indicating that surface charge was only generated through ion adsorption from the electrolyte solution. The IEP of the untreated sample was located at a pH of 3.6. The treated sample showed a flatter curve with the IEP shifting to a pH of 2.7.

While the contact-angle measurements showed broadly similar behavior for MABS and PU apart from the contact-angle hysteresis, the zeta-potential measurements showed a clear difference in behavior between the materials. MABS samples were unaffected by the

gas treatment. PU, on the other hand, showed substantial changes. The potential curve was flattened to reflect the increased hydrophilicity of the sample surface [50]. The IEP moved from a pH value of 3.6 to 2.7. This suggested the formation of acidic species on the PU surface (Figure 7c) [51]. A comparison between the zeta-potential and the FTIR-ATR results of both compounds (Figure 2, Figure 3, and Figure 7b,c) led to the conclusion that the most influential was the adsorbed HNO₃. The attribution of the surface effects to the adsorbed HNO₃ was supported by the simultaneous increase in both acidity and hydrophilicity exhibited by PU (Figure 7c). This result also supported the attribution of contact-angle decrease to the HNO₃ adsorption in the paragraphs following Figure 6. The difference between MABS and PU likely resulted from different HNO₃ surface concentrations after the NO treatment. The differences in signal height development between both compounds are unlikely to have played a significant role, as the time frame of the zeta-potential measurements was much shorter than the liquid immersion experiments. A comparison of the signal heights at 3480/3443 cm⁻¹ showed a significantly higher signal with PU than with MABS (Figure 3a,c, and Figure 4a,c). The HNO₃ surface concentration of MABS was too low to influence the potential curve. In contrast, the surface concentration of PU was high enough to impact the zeta-potential measurements.

4. Conclusions

This paper showed the impact of NO treatment on the surface properties of several polymers and the stability of these effects under liquid contact. The measurements showed that the gas treatment had little to no impact on PMP. The surfaces of MABS became more hydrophilic and chemically heterogeneous, while PU became more hydrophilic and acidic based on both the contact-angle and zeta-potential measurements. The increase in hydrophilicity of both MABS and PU was mainly due to the adsorption of HNO₃. The formation of nitro and nitrate ester groups was stable on both MABS and PU surfaces, with the adsorbed HNO₃ molecules proving less stable.

The results discussed in this paper point to an overall positive outlook for applying nitric oxide in the ECMO circuit. The major blood-contacting surface PMP showed little to no changes. The other two blood-contacting surfaces, MABS and PU, developed functional groups largely stable under liquid contact, indicating a low risk for patients during application. However, this is just an initial observation, as blood represents a significantly more complex system than the liquids used in the experiments discussed in this publication. The surfaces became more hydrophilic, potentially improving their liquid contact and hemocompatibility properties [14].

Supplementary Materials: The following supporting information can be downloaded at <https://www.mdpi.com/article/10.3390/app15052646/s1>: Figure S1: Complete FTIR-ATR spectra of PMP treated with NO (1000 ppm) for 17 h immersed in either (a) Millipore water or (b) physiological saline solution; Figure S2: Complete FTIR-ATR spectra of MABS treated with NO (1000 ppm) for 17 h immersed in either (a) Millipore water or (b) physiological saline solution; Figure S3: Complete FTIR-ATR spectra of PU treated with NO (1000 ppm) for 17 h immersed in either (a) Millipore water or (b) physiological saline solution; Table S1: Characteristic photograph of the contact-angle measurements of the hollow fiber membranes; Table S2: Individual advancing and receding angles of the untreated hollow fiber membrane (PMP) samples; Table S3: Individual advancing and receding angles of the hollow fiber membrane (PMP) samples treated with NO (1000 ppm) for 17 h; Table S4: Individual advancing and receding angles of the inlet/outlet cap (MABS) samples both untreated and treated with NO (1000 ppm) for 17 h (* no receding angle; continuous decline with decreasing radius); Table S5: Individual advancing and receding angles of the PU material samples both untreated and treated with NO (1000 ppm) for 17 h; Scheme S1: Potential reaction mechanism for the formation of nitro and nitrite ester groups through electrophilic addition of NO₂ [36,37]; Scheme S2:

Reaction mechanism for the crosslinking and chain scission reactions of the carbamate group caused by NO₂ [38]; Scheme S3: Potential reaction mechanism for the formation of nitro groups through the electrophilic aromatic nitration reaction, which occurs in a continuum between a polar and a single electron charge transfer (SET) mechanism [40,52,53]; Scheme S4: Potential reaction mechanism for the formation of nitrate ester groups from nitrite ester groups [36,41]; Scheme S5: Potential reaction mechanisms for the formation of nitrate ester groups through the reaction of nitric acid with hydroxy groups [42,54]; Scheme S6: Acid-catalyzed ester hydrolysis mechanism [55].

Author Contributions: M.K.: Formal analysis (equal), investigation (equal), methodology (equal), data curation (equal), visualization (lead), writing—original draft (lead). A.C.: Formal analysis (equal), data curation (equal), investigation (equal). S.M.: Formal analysis (equal), data curation (equal), investigation (equal). G.K.A.: Supervision (equal), writing—review and editing (equal). W.K.: Supervision (equal), conceptualization (equal), writing—review and editing (equal). All authors have read and agreed to the published version of the manuscript.

Funding: This research was supported by the ZIM program (Zentrales Innovationsprogramm Mittelstand or Central Innovation Program for small- and medium-sized enterprises (SMEs)) of the Federal Ministry for Economic Affairs and Climate Action under the research project “NOAMED—Stickstoffmonoxid zur Oberflächenmodifikation beim Einsatz von Gasaustauschern bei der extrakorporalen Lungenunterstützung” (KK 5023802AD0) conducted in cooperation with Hemovent GmbH (Aachen, Germany).

Institutional Review Board Statement: Not applicable.

Data Availability Statement: The original contributions presented in this study are included in the article/Supplementary Material. Further inquiries can be directed to the corresponding author.

Acknowledgments: The authors would like to thank Hemovent GmbH for the close cooperation and advice throughout the research project and for providing the experimental materials.

Conflicts of Interest: The authors declare that they have no known competing financial interests or personal relationships that could have influenced the work reported in this paper.

References

1. Makdisi, G.; Wang, I.-W. Extra Corporeal Membrane Oxygenation (ECMO) review of a lifesaving technology. *J. Thorac. Dis.* **2015**, *7*, E166–E176. [[CrossRef](#)] [[PubMed](#)]
2. Banfi, C.; Pozzi, M.; Siegenthaler, N.; Brunner, M.-E.; Tassaux, D.; Obadia, J.-F.; Bendjelid, K.; Giraud, R. Veno-venous extracorporeal membrane oxygenation: Cannulation techniques. *J. Thorac. Dis.* **2016**, *8*, 3762–3773. [[CrossRef](#)] [[PubMed](#)]
3. Allen, S.; Holena, D.; McCunn, M.; Kohl, B.; Sarani, B. A Review of the Fundamental Principles and Evidence Base in the Use of Extracorporeal Membrane Oxygenation (ECMO) in Critically Ill Adult Patients. *J. Intensive Care Med.* **2011**, *26*, 13–26. [[CrossRef](#)] [[PubMed](#)]
4. Zeibi Shirejini, S.; Carberry, J.; McQuilten, Z.K.; Burrell, A.J.C.; Gregory, S.D.; Hagemeyer, C.E. Current and future strategies to monitor and manage coagulation in ECMO patients. *Thrombosis J.* **2023**, *21*, 11. [[CrossRef](#)]
5. Karagiannidis, C.; Strassmann, S.; Larsson, A.; Brodie, D. The Hemovent Oxygenator: A New Low-Resistance, High-Performance Oxygenator. *ASAIO J.* **2021**, *67*, e59–e61. [[CrossRef](#)]
6. Olson, S.R.; Murphree, C.R.; Zonies, D.; Meyer, A.D.; Mccarty, O.J.T.; Deloughery, T.G.; Shatzel, J.J. Thrombosis and Bleeding in Extracorporeal Membrane Oxygenation (ECMO) Without Anticoagulation: A Systematic Review. *ASAIO J.* **2021**, *67*, 290–296. [[CrossRef](#)]
7. Gajkowski, E.F.; Herrera, G.; Hatton, L.; Velia Antonini, M.; Vercaemst, L.; Cooley, E. ELSO Guidelines for Adult and Pediatric Extracorporeal Membrane Oxygenation Circuits. *ASAIO J.* **2022**, *68*, 133–152. [[CrossRef](#)] [[PubMed](#)]
8. Andrabi, S.M.; Sharma, N.S.; Karan, A.; Shahriar, S.M.S.; Cordon, B.; Ma, B.; Xie, J. Nitric Oxide: Physiological Functions, Delivery, and Biomedical Applications. *Adv. Sci.* **2023**, *10*, e2303259. [[CrossRef](#)]
9. Jin, R.C.; Loscalzo, J. Vascular Nitric Oxide: Formation and Function. *J. Blood Med.* **2010**, *2010*, 147–162. [[CrossRef](#)]
10. Köglmaier, M.; Joost, T.; Kronseder, M.; Kunz, W. Characterization of the interaction of nitric oxide/nitrogen dioxide with the polymer surfaces in ECMO devices. *J. Polym. Res.* **2024**, *31*, 261. [[CrossRef](#)]

11. Obstals, F.; Vorobii, M.; Riedel, T.; de Los Santos Pereira, A.; Bruns, M.; Singh, S.; Rodriguez-Emmenegger, C. Improving Hemocompatibility of Membranes for Extracorporeal Membrane Oxygenators by Grafting Nonthrombogenic Polymer Brushes. *Macromol. Biosci. [Online]* **2018**, *18*, 1700359. [[CrossRef](#)] [[PubMed](#)]
12. Lim, M.W. The history of extracorporeal oxygenators. *Anaesthesia* **2006**, *61*, 984–995. [[CrossRef](#)]
13. O'Brien, C.; Monteagudo, J.; Schad, C.; Cheung, E.; Middlesworth, W. Centrifugal pumps and hemolysis in pediatric extracorporeal membrane oxygenation (ECMO) patients: An analysis of Extracorporeal Life Support Organization (ELSO) registry data. *J. Pediatr. Surg.* **2017**, *52*, 975–978. [[CrossRef](#)] [[PubMed](#)]
14. Karagiannidis, C.; Joost, T.; Strassmann, S.; Weber-Carstens, S.; Combes, A.; Windisch, W.; Brodie, D. Safety and Efficacy of a Novel Pneumatically Driven Extracorporeal Membrane Oxygenation Device. *Ann. Thorac. Surg.* **2020**, *109*, 1684–1691. [[CrossRef](#)]
15. Menninger, L.; Körner, A.; Mirakaj, V.; Heck-Swain, K.-L.; Haeberle, H.A.; Althaus, K.; Baumgaertner, M.; Jost, W.; Schlensak, C.; Rosenberger, P.; et al. Membrane oxygenator longevity was higher in argatroban-treated patients undergoing vvECMO. *Eur. J. Clin. Investig.* **2023**, *53*, e13963. [[CrossRef](#)] [[PubMed](#)]
16. O'Meara, C.; Timpa, J.; Peek, G.; Sindelar, M.; Ross, J.; Raper, J.; Byrnes, J.W. Nitric Oxide on Extracorporeal Life Support-Circuit Modifications for a Safe Therapy. *J. Extra-Corpor. Technol.* **2022**, *54*, 142–147. [[CrossRef](#)]
17. Winnersbach, P.; Hosseinnejad, A.; Breuer, T.; Fechter, T.; Jakob, F.; Schwaneberg, U.; Rossaint, R.; Bleilevens, C.; Singh, S. Endogenous Nitric Oxide-Releasing Microgel Coating Prevents Clot Formation on Oxygenator Fibers Exposed to In Vitro Blood Flow. *Membranes* **2022**, *12*, 73. [[CrossRef](#)]
18. Taite, L.J.; Yang, P.; Jun, H.-W.; West, J.L. Nitric oxide-releasing polyurethane-PEG copolymer containing the YIGSR peptide promotes endothelialization with decreased platelet adhesion. *J. Biomed. Mater. Res. B Appl. Biomater.* **2008**, *84*, 108–116. [[CrossRef](#)]
19. Brinkley, L.; Brock, M.A.; Stinson, G.; Bilgili, A.; Jacobs, J.P.; Bleiweis, M.; Peek, G.J. The biological role and future therapeutic uses of nitric oxide in extracorporeal membrane oxygenation, a narrative review. *Perfusion* **2025**, *40*, 83–91. [[CrossRef](#)]
20. Malfertheiner, M.V.; Garrett, A.; Passmore, M.; Haymet, A.B.; Webb, R.I.; Bahr, V.V.; Millar, J.E.; Schneider, B.A.; Obonyo, N.G.; Black, D.; et al. The effects of nitric oxide on coagulation and inflammation in ex vivo models of extracorporeal membrane oxygenation and cardiopulmonary bypass. *Artif. Organs* **2023**, *47*, 1581–1591. [[CrossRef](#)]
21. Lopez, L.C.; Wilkes, G.L.; Stricklen, P.M.; White, S.A. Synthesis, Structure, and Properties of Poly(4-Methyl-1 -Pentene). *J. Macromol. Sci. Polymer Rev.* **1992**, *32*, 301–406. [[CrossRef](#)]
22. Stamm, M. (Ed.) *Polymer Surfaces and Interfaces: Characterization, Modification and Applications*; Springer: Berlin, Heidelberg, 2008.
23. Xu, L.; Tang, Q.; Liu, B.; Zhang, M. Control of the composition of matrix resin for the design of MABS resin with good transparency and toughness. *Colloids Surf. A Physicochem. Eng. Asp.* **2023**, *658*, 130608. [[CrossRef](#)]
24. Riley, B.; Sapatnekar, S.; Cornell, D.T.; Anderson, J.; Walsh-sukys, M. Impact of prolonged saline solution prime exposure on integrity of extracorporeal membrane oxygenation circuits. *J. Perinatol.* **1997**, *17*, 444–449.
25. Larkin, P. *Infrared and Raman Spectroscopy. Principles and Spectral Interpretation*, 2nd ed.; Elsevier: Amsterdam, The Netherlands, 2018.
26. Schnitzer, C.; Ripperger, S. Influence of Surface Roughness on Streaming Potential Method. *Chem. Eng. Technol.* **2008**, *31*, 1696–1700. [[CrossRef](#)]
27. Bellmann, C.; Caspari, A.; Albrecht, V.; Loan Doan, T.T.; Mäder, T.; Luxbacher, T.; Kohl, R. Electrokinetic properties of natural fibres. *Colloids Surf. A Physicochem. Eng. Asp.* **2005**, *267*, 19–23. [[CrossRef](#)]
28. Huhtamäki, T.; Tian, X.; Korhonen, J.T.; Ras, R.H.A. Surface-wetting characterization using contact-angle measurements. *Nat. Protoc.* **2018**, *13*, 1521–1538. [[CrossRef](#)] [[PubMed](#)]
29. Hebbar, R.S.; Isloor, A.M.; Ismail, A.F. Chapter 12-Contact Angle Measurements. In *Membrane Characterization*; Hilal, N., Ismail, A.F., Matsuura, T., Oatley-Radcliffe, D., Eds.; Elsevier: Amsterdam, The Netherlands, 2017; pp. 219–255.
30. Wang, J.; Wu, Y.; Cao, Y.; Li, G.; Liao, Y. Influence of surface roughness on contact angle hysteresis and spreading work. *Colloid Polym. Sci.* **2020**, *298*, 1107–1112. [[CrossRef](#)]
31. Drechsler, A.; Frenzel, R.; Caspari, A.; Michel, S.; Holzschuh, M.; Synytska, A.; Curosu, I.; Liebscher, M.; Mechtcherine, V. Surface modification of poly(vinyl alcohol) fibers to control the fiber-matrix interaction in composites. *Colloid Polym. Sci.* **2019**, *297*, 1079–1093. [[CrossRef](#)]
32. Della Volpe, C.; Siboni, S. The Wilhelmy method: A critical and practical review. *Surf. Innov.* **2018**, *6*, 120–132. [[CrossRef](#)]
33. Socrates, G. *Infrared and Raman Characteristic Group Frequencies. Tables and Charts*, 3rd ed.; repr. as paperback; Wiley: Chichester, UK, 2010.
34. Tsukahara, H.; Ishida, T.; Mayumi, M. Gas-Phase Oxidation of Nitric Oxide: Chemical Kinetics and Rate Constant. *Nitric Oxide* **1999**, *3*, 191–198. [[CrossRef](#)]
35. England, C.; Corcoran, W.H. Kinetics and Mechanisms of the Gas-Phase Reaction of Water Vapor and Nitrogen Dioxide. *Ind. Eng. Chem. Fund.* **1974**, *13*, 373–384. [[CrossRef](#)]
36. Ogihara, T. Oxidative Degradation of Polyethylene in Nitrogen Dioxide. *Bull. Chem. Soc. Jpn.* **1963**, *36*, 58–63. [[CrossRef](#)]

37. Giamalva, D.H.; Kenion, G.B.; Church, D.F.; Pryor, W.A. Rates and mechanisms of reactions of nitrogen dioxide with alkenes in solution. *J. Am. Chem. Soc.* **1987**, *109*, 7059–7063. [[CrossRef](#)]
38. Pariiskii, G.B.; Gaponova, I.S.; Davydov, E.Y. Reactions of nitrogen oxides with polymers. *Russ. Chem. Rev.* **2000**, *69*, 985–999. [[CrossRef](#)]
39. Jellinek, H.H.G.; Wang, T.J.Y. Reaction of nitrogen dioxide with linear polyurethane. *J. Polym. Sci. Polym. Chem. Ed.* **1973**, *11*, 3227–3242. [[CrossRef](#)]
40. Ridd, J.H. Mechanism of aromatic nitration. *Acc. Chem. Res.* **1971**, *4*, 248–253. [[CrossRef](#)]
41. Gray, P.; Williams, A. The thermochemistry and reactivity of alkoxy radicals. *Chem. Rev.* **1959**, *59*, 239–328. [[CrossRef](#)]
42. Boschan, R.; Mellow, R.T.; van Dolah, R.W. The Chemistry of Nitrate Esters. *Chem. Rev.* **1955**, *55*, 485–510. [[CrossRef](#)]
43. Li, G.-B.; Cai, S.-H.; Long, B. New Reactions for the Formation of Organic Nitrate in the Atmosphere. *ACS Omega* **2022**, *7*, 39671–39679. [[CrossRef](#)]
44. Martínez, I.; Casas, P.A. Simple model for CO₂ absorption in a bubbling water column. *Braz. J. Chem. Eng.* **2012**, *29*, 107–111. [[CrossRef](#)]
45. Keshavarz, F.; Thornton, J.A.; Vehkamäki, H.; Kurtén, T. Reaction Mechanisms Underlying Unfunctionalized Alkyl Nitrate Hydrolysis in Aqueous Aerosols. *ACS Earth Space Chem.* **2021**, *5*, 210–225. [[CrossRef](#)]
46. Khalil, F.Y.; Hanna, M.T. Kinetic salt effects in the acid hydrolysis of potassium ethyl malonate in water and in 50% dioxane? Water mixture. *Monatsh. Chem.* **1980**, *111*, 841–849. [[CrossRef](#)]
47. Kwok, D.Y.; Gietzelt, T.; Grundke, K.; Jacobasch, H.-J.; Neumann, A.W. Contact Angle Measurements and Contact Angle Interpretation. 1. Contact Angle Measurements by Axisymmetric Drop Shape Analysis and a Goniometer Sessile Drop Technique. *Langmuir* **1997**, *13*, 2880–2894. [[CrossRef](#)]
48. Lam, C.; Ko, R.; Yu, L.; Ng, A.; Li, D.; Hair, M.L.; Neumann, A.W. Dynamic Cycling Contact Angle Measurements: Study of Advancing and Receding Contact Angles. *J. Colloid Interface Sci.* **2001**, *243*, 208–218. [[CrossRef](#)]
49. Marmur, A. Solid-Surface Characterization by Wetting. *Annu. Rev. Mater. Res.* **2009**, *39*, 473–489. [[CrossRef](#)]
50. Temmel, S.; Kern, W.; Luxbacher, T. Zeta Potential of Photochemically Modified Polymer Surfaces. In *Characterization of Polymer Surfaces and Thin Films*; Grundke, K., Stamm, M., Adler, H.-J., Eds.; Progress in Colloid and Polymer Science; Springer: Berlin/Heidelberg, Germany, 2006; pp. 54–61.
51. Nygård, P.; Grundke, K.; Mäder, E.; Bellmann, C. Wetting kinetics and adhesion strength between polypropylene melt and glass fibre: Influence of chemical reactivity and fibre roughness. *J. Adhes. Sci. Technol.* **2002**, *16*, 1781–1808. [[CrossRef](#)]
52. De Queiroz, J.F.; Carneiro, J.W.d.M.; Sabino, A.A.; Sparrapan, R.; Eberlin, M.N.; Esteves, P.M. Electrophilic aromatic nitration: Understanding its mechanism and substituent effects. *J. Org. Chem.* **2006**, *71*, 6192–6203. [[CrossRef](#)]
53. Liljenberg, M.; Stenlid, J.H.; Brinck, T. Mechanism and regioselectivity of electrophilic aromatic nitration in solution: The validity of the transition state approach. *J. Mol. Model.* **2017**, *24*, 15. [[CrossRef](#)]
54. Urbański, T. *Chemistry and Technology of Explosives*; Repr; Pergamon Pr: Oxford, UK, 1983.
55. Shi, H.; Wang, Y.; Hua, R. Acid-catalyzed carboxylic acid esterification and ester hydrolysis mechanism: Acylium ion as a sharing active intermediate via a spontaneous trimolecular reaction based on density functional theory calculation and supported by electrospray ionization-mass spectrometry. *Phys. Chem. Chem. Phys.* **2015**, *17*, 30279–30291. [[CrossRef](#)]

Disclaimer/Publisher’s Note: The statements, opinions and data contained in all publications are solely those of the individual author(s) and contributor(s) and not of MDPI and/or the editor(s). MDPI and/or the editor(s) disclaim responsibility for any injury to people or property resulting from any ideas, methods, instructions or products referred to in the content.